Available online at www.sciencedirect.com
ScienceDirect
Geochimica et Cosmochimica Acta 74 (2010) 1551–1562
Geochimica et Cosmochimica Acta
www.elsevier.com/locate/gca

Uptake of uranium and trace elements in pyrite (FeS_2) suspensions

M. Descostes [a,b,1], M.L. Schlegel [b,c,*], N. Eglizaud [a,2], F. Descamps [a], F. Miserque [c], E. Simoni [d]

[a] CEA, DEN, DPC/SECR/Laboratory of Radionuclides Migration Measurements and Modelling, F-91191 Gif-sur-Yvette, France
[b] University of Evry, UMR 8587 LAMBE, F-91025 Evry, France
[c] CEA, DEN, DPC/SCP/Laboratory for the Reactivity of Surfaces and Interfaces, F-91191 Gif-sur-Yvette, France
[d] University of Paris-Sud 11, Institut de Physique Nucléaire, F-91406 Orsay, France

Received 9 June 2009; accepted in revised form 30 November 2009; available online 5 January 2010

Abstract

Pyrite dissolution and interaction with $Fe^{(II)}$, $Co^{(II)}$, $Eu^{(III)}$ and $U^{(VI)}$ have been studied under anoxic conditions by solution chemistry and spectroscopic techniques. Aqueous data show a maximal cation uptake above pH 5.5. Iron (II) uptake can explain the non-stoichiometric $[S]_{aq}/[Fe]_{aq}$ ratios often observed during dissolution experiments. Protonation data corrected for pyrite dissolution resulted in a proton site density of 9 ± 3 sites nm^{-2}. Concentration isotherms for $Eu^{(III)}$ and $U^{(VI)}$ sorption on pyrite indicate two different behaviours which can be related to the contrasted redox properties of these elements. For $Eu^{(III)}$, sorption can be explained by the existence of a unique site with a saturation concentration of 1.25×10^{-6} mol g^{-1}. In the $U^{(VI)}$ case, sorption seems to occur on two different sites with a total saturation concentration of 4.5×10^{-8} mol g^{-1}. At lower concentration, uranium reduction occurs, limiting the concentration of dissolved uranium to the solubility of UO_2(s).

Scanning electron microscopy and micro-Raman spectrometry of $U^{(VI)}$-sorbed pyrite indicate a heterogeneous distribution of U at the pyrite surface and a close association with oxidized S. X-ray photoelectron spectroscopy confirms the partial reduction of U and the formation of a hyperstoichiometric UO_{2+x}(s). Our results are consistent with a chemistry of the pyrite surface governed not by $Fe^{(II)}$-bound hydroxyl groups, but by S groups which can either sorb cations and protons, or sorb and reduce redox-sensitive elements such as $U^{(VI)}$.
© 2009 Elsevier Ltd. All rights reserved.

1. INTRODUCTION

Several European countries are studying the disposal of nuclear waste in deep geological repositories embedded in clay rocks, such as Opalinus Clay in Switzerland (NAGRA, 2002), Callovo-Oxfordian argillite in France (ANDRA, 2005), and Boom Clay in Belgium (ONDRAF, 2001). Corrosion of waste containers and alteration of waste forms will ultimately lead to radionuclide (RN) release and migration in the geological formations. However, this migration can be slowed down by RN partitioning to solids. Consequently, RN adsorption on solid phases by ligand exchange, ion exchange, specific sorption or (co)precipitation has been extensively explored. In contrast, retention coupled with redox reactions has scarcely been studied, despite the ubiquitous presence of redox-sensitive minerals such as pyrite (FeS_2) in clay formations.

Pyrite is known to buffer reducing conditions in clay formations (Beaucaire et al., 2000, 2008; Gaucher et al., 2006). Because of its surface reactivity, several studies have been devoted to the sorption properties of FeS_2. Many of these studies focused on the sorption of cations (Jean and Bancroft, 1986; Hyland and Bancroft, 1990; Hyland et al., 1990; Kornicker and Morse, 1991; Scaini et al., 1995; Bostick et al., 2000; Ehrhardt et al., 2000). This cation affinity could be partly explained by the very low point of zero charge (pH_{PZC}) of pyrite which is usually estimated to a

* Corresponding author. Address: University of Evry, UMR 8587 LAMBE, F-91025 Evry, France. Tel.: +33 1 69 08 93 84.
E-mail address: michel.schlegel@cea.fr (M.L. Schlegel).
[1] Present address: AREVA NC, Mining Business Unit, F-92084 Paris la Défense, France.
[2] Present address: EDF-CNEN, F-92120 Montrouge, France.

0016-7037/$ - see front matter © 2009 Elsevier Ltd. All rights reserved.
doi:10.1016/j.gca.2009.12.004

value lower than 2 (Fornasiero et al., 1992; Bebié et al., 1998). Sorption and reduction were observed for redox-sensitive cations such as Au, Ag, Pd and Hg. These coupled sorption–reduction processes can be explained by two distinct mechanisms. The first mechanism implies the formation of M_xS surface species, and subsequent electron transfer coupled to disproportionation of the pyrite $S_2^{(-II)}$ moiety. The second mechanism relies on pyrite oxidation directly by the sorbed cation (Jean and Bancroft, 1986; Hyland and Bancroft, 1990; Scaini et al., 1995).

An accurate identification of the actual sorption mechanisms operating at the sulphide surface requires that extreme care should be taken to avoid pyrite oxidation by molecular O_2 prior to or during uptake experiments. Otherwise, the observed macroscopic sorption may actually occur on the surface of pyrite oxidation products (ferric oxyhydroxides and oxides) rather than on the pyrite pristine surface. This is especially true for $U^{(VI)}$, which is known to be efficiently scavenged by Fe (hydr)oxides (e.g., Hsi and Langmuir, 1985; Waite et al., 1994; Gabriel et al., 1998; Lenhart and Honeyman, 1999; Murphy et al., 1999; Dodge et al., 2002; Missana et al., 2003; Guo et al., 2009). Yet Scott et al. (2007) recently indicated that freshly polished pyrite surfaces exhibit higher $U^{(VI)}$ uptake than weathered surfaces, motivating a direct probe of the interaction between clean pyrite and $U^{(VI)}$.

Uranium is an element of interest for both the deep disposal of nuclear waste and for remediation of contaminated surface sites. Studies of $U^{(VI)}$ interaction with $Fe^{(II)}$-bearing phases such as magnetite indicate that $U^{(VI)}$ can simply adsorb, but also can be subsequently reduced to $U^{(IV)}$ and precipitate as hyperstoichiometric UO_{2+x} (Grambow et al., 1996; Scott et al., 2005; El Aamrani et al., 2007). Uranium reactivity with pyrite has scarcely been studied, and most studies were performed in the pH range of roughly 4.8–6, and high U concentration, somewhat above the solubility of schoepite (Wersin et al., 1994; Aubriet et al., 2006; Eglizaud et al., 2006; Scott et al., 2007). Therefore, even if sorption occurred, it is rather difficult to extend their results to lower concentration.

This study aims at understanding the interaction between $U^{(VI)}$ and the pyrite surface with a special emphasis on the aqueous speciation and pyrite surface characterization. In order to complete our understanding of pyrite sorption properties, sorption of $Eu^{(III)}$, often taken as an actinide analogue, and of $Co^{(II)}$ and $Fe^{(II)}$ were also studied.

2. MATERIALS AND METHODS

A detailed description of all materials and methods used in this study can be found in Eglizaud (2006). Pyrite preparation and sorption studies were performed in anoxic glove boxes with a N_2 atmosphere and O_2 partial pressure (P_{O2}) below 1 ppm. The low P_{O2} was maintained by continuously recirculating the glove box atmosphere on O_2 traps. All solutions were prepared with deionized water (Milli-Q) and chemicals of ACS reagent grade. Water was degassed by bubbling pure N_2 (99.9999%) prior to introduction in the glove box. This bubbling efficiently removed O_2, as proved by the absence of P_{O2} increase when introducing water in the glove box (Eglizaud, 2006).

2.1. Pyrite preparation and characterization

Natural pyrite crystals (cubic, edges of about 2 cm) from Logroño (Spain) and devoid of chemical zoning were selected for this study. Initial characterization of the raw cubes was performed by Scanning Electron Microscopy (SEM; JEOL 6100 microscope) coupled with Energy Dispersive X-ray Spectrometry (EDS, Noran spectrometer). The electron beam was accelerated to 15 keV, allowing elemental analysis of pyrite to a depth of ~1.8 μm representative of the solid bulk. These analyses showed that the Fe/S elemental ratio equalled 0.5, in agreement with the pyrite stoichiometry. The mineralogy and absence of other mineral phases on ground pyrite were verified by X-Ray Diffraction (XRD) using a Philips X'pert diffractometer with a Co anode operated at 40 mA and 40 kV. Mineral impurities (phyllosilicate) could be detected only in trace amounts ($\leqslant$1% for pristine pyrite).

Pyrite crystals were introduced into the glove box and then dipped in 37% HCl for several hours to remove any oxidation products present at the mineral surface. The pyrite was rinsed with acetone, then grounded in a ball mill and sieved to recover the 25–50 μm and 50–150 μm fractions. These powders were suspended in ethanol, sonicated, allowed to settle, and the supernatant discarded to remove any fine particles adhering to the grain surfaces. These operations were repeated until no particle was observed anymore in ethanol after sonication, as confirmed by SEM. X-ray diffraction of the purified powder showed that >90% of the mineral impurities were removed by this preparation protocol. The remaining ancillary particles were probably occluded in the pyrite solid, hence they cannot react with the supernatant. Moreover, the XPS survey spectrum of prepared pyrite showed only contributions from reduced S and $Fe^{(II)}$, meaning that the surface is free from these mineral contaminants. The mineral purity was also checked by micro-Raman (μRaman) spectroscopy (see below). Prepared powders were stored in an anoxic glove box. The specific surface area of the pyrite powder was measured by BET multipoint analysis on the 50–150 μm fraction (Micromeritics ASAP2010) using Kr gas and equalled 0.060 ± 0.004 m^2 g^{-1}.

2.2. Solid characterization

X-ray photoelectron spectra of unreacted and $U^{(VI)}$-reacted pyrite were measured on a VG 220 iXL Escalab spectrometer, with an Al Kα monochromated source (1486.6 eV). Powders of reacted pyrite were fixed with a carbon adhesive, and surfaces of 1 mm^2 were probed, with a spectral resolution of 0.3 eV. The energy scale for each spectrum was calibrated by setting the C-1s peak from contamination carbon at 284.6 eV. The Fe-2p, S-2p and U-4f bands were recorded with high-resolution scans (pass energy of 20 eV). Because Binding Energies (BE) in the literature are somewhat scattered for Fe and S compounds, some reference compounds were also measured by XPS to complete the consistent database of previously published BE (Descostes et al., 2000). These solid compounds were FeO, α-Fe_2O_3, and α-FeOOH (Sigma–Aldrich). To avoid

the accumulation of electronic charges during spectral acquisition, however, photoelectron spectra for these references were recorded with a non-monochromatized X-ray source. This leads to broader peaks in the XPS spectra of the reference compounds. Spectral decomposition was performed with the Avantage software using a Shirley background and a Gaussian/Lorentzian (G/L) ratio of 70/30. For U, an additional mixed approach was used, in which part of the XPS contribution was modelled using an experimental spectrum from $UO_2(OH)_2$(s). This allows to directly single out contributions at low BE.

Micro-Raman spectrometry was performed on a HoloLab 5000 spectrometer combined with an Olympus BX60 microscope. A frequency-doubled (532 nm) Nd:YAG laser was used for excitation, and delivered a power of about 10–12 mW on the sample. The laser light was focused on the sample using magnification lens of 10× to 50×, leading to a probed area of $\sim 30 \times 20\ \mu m^2$ down to $6 \times 6\ \mu m^2$. Samples were analyzed in air during a period of 15 min to limit oxidation. Several scans of 1 s each were collected, corrected for the contribution from the electronic setup, and summed together. Spectra were also collected for S reference compounds (S^0, $S_2O_3^{2-}$, $S_4O_6^{2-}$, SO_3^{2-} and SO_4^{2-}). Reference Raman spectra for UO_{2+x} and Fe compounds were taken from the literature (Dunn et al., 2000; Manara and Renker, 2003). Finally, SEM imaging and EDS of reacted pyrite was performed with an electron beam accelerated to 10–15 keV allowing elemental analysis of pyrite to a depth between 0.9 and 1.8 μm.

2.3. Electrophoresis experiments

The experimental protocol is adapted from previous studies (Fornasiero et al., 1992; Bebié et al., 1998; Vergouw et al., 1998). Two size fractions (25–50 μm and 50–150 μm) were tested. Pyrite suspensions were first prepared in an anoxic glove box and equilibrated at pH 2 during 16 h. Then the solids were decanted and rinsed three times with solution adjusted at the desired pH (from 2 to 7.5). Measurements were performed on a Zetasizer ZEM 5000 (Malvern) apparatus. The Zetamaster cell and the injection loop were both initially rinsed with 2 mL of the studied solution, then 5 mL of suspension were introduced with a syringe. Measurements were repeated between 10 and 20 times.

2.4. Potentiometric titrations

For titration, aqueous suspensions of $8\ g\ L^{-1}$ pyrite in $0.01\ mol\ L^{-1}$ $NaNO_3$ were first equilibrated at pH 2 (0.01 M HNO_3) during 4 h. After equilibration, the suspensions were titrated by adding incremental volumes of 0.1 M NaOH. pH values were accepted for pH drifts of $\leqslant 0.01$ pH unit/min. Blank titrations were performed in pure $0.01\ mol\ L^{-1}$ $NaNO_3$ solutions. From the difference in titration data of the suspension and the blank, an excess of proton release was calculated. Note that this excess corresponds to deprotonation reactions at the pyrite surface, but also to acido-basic reactions of dissolved species. Hence, the apparent excess of proton release had to be corrected for the presence of dissolved Fe^{2+}, for HSO_4^-/SO_4^{2-} ($pK_a = 1.99$), and for H^+ produced by pyrite oxidative dissolution. The corrected value was assumed to represent the concentration of sorption sites in the suspension ([sites]), and was used to calculate the surface site density (d, sites nm^{-2}) according to

$$d = \frac{[\text{sites}] \times N_A}{t \times S_{BET} \times 10^{18}} \quad (1)$$

where t is the solid/water ratio ($g\ L^{-1}$), S_{BET} is the specific area ($m^2\ g^{-1}$) and N_A the Avogadro number.

2.5. Uptake experiments

Uptake experiments of $Fe^{(II)}$, $Co^{(II)}$, $Eu^{(III)}$ and $U^{(VI)}$ were performed in $8\ g\ L^{-1}$ pyrite suspensions at buffered ionic strength ($0.01\ mol\ L^{-1}$ $NaNO_3$; Merck Suprapur) in HDPE vials. Sorption isotherms as a function of pH were obtained for initial cation concentrations of $2 \times 10^{-6}\ mol\ L^{-1}$ for $Fe^{(II)}$ and $Co^{(II)}$, and $4 \times 10^{-8}\ mol\ L^{-1}$ for $U^{(VI)}$ and $Eu^{(III)}$. These low concentrations were selected to be under the solubility of any studied cation and to compare with the amount of proton sites determined by titration (see Section 3). Sorption isotherms as a function of cation concentration were also performed at given pH. Uranium (VI) was introduced as an uranyl nitrate solution (Sigma–Aldrich). Cobalt (II) sorption was probed using ^{60}Co radiotracer (CERCA ELSB45, $CoCl_3$ solution). Europium (III) uptake was studied either with ^{152}Eu radiotracer (CERCA ELSB50, $EuCl_3$ solution) or stable Eu from an ICP-MS standard solution (PlasmaCAL SCP Science, 1000 $\mu g\ mL^{-1}$). Iron (II) sorption was studied with ^{55}Fe radiotracer (CERCA ELSB45, $FeCl_3$ solution). A solution of $[Fe^{(II)}] = (1.05 \pm 0.03) \times 10^{-4}\ mol\ L^{-1}$ was obtained by reducing $^{55}Fe^{(III)}$ by H_2(g) bubbling in presence of $Fe^{(0)}$. That $Fe^{(II)}$ was reduced was checked by UV–vis spectrophotometry using the ferrozin method (Viollier et al., 2000). In parallel to uptake suspensions, blank suspensions (with pyrite, without sorbate) were also prepared and reacted. To verify the absence of Na sorption on pyrite, uptake experiments were performed with ^{22}Na radiotracer (ELSA50, CERCA). No ^{22}Na sorption could be detected, contrary to the results reported by Kornicker and Morse (1991).

For uptake experiments, suspension pH was first adjusted with NaOH (Aldrich Suprapur) or HNO_3 (ULTREX II, J.T. Baker). An aliquot of the tracer solutions was then added to the uptake vials. The vials were stoppered and continuously shaken. The samples were left to equilibrate for a period of 48 h, after which no more uptake could be observed. The supernatant was recovered by filtration (0.2 μm) and acidified. Dissolved Fe and S concentrations in the supernatant ($[Fe]_{aq}$ and $[S]_{aq}$, respectively) were followed for some experiments with or without sorption tracers. Supernatants were analyzed by ICP-OES (Perkin-Elmer Optima 2000 DV). The oxidation state of aqueous Fe was determined by UV–vis spectrophotometry using the ferrozin method. The ^{55}Fe supernatants were counted by β liquid scintillation (Packard Tri-Carb 2500), and ^{22}Na, ^{152}Eu and ^{60}Co were determined by γ spectrometry (Perkin-Elmer Wallac 1480). The counting efficiency for each tracer was measured by running blank preparations,

and data were corrected for radioactive decay. U and stable Eu analyses were performed by ICP-MS (ThermoVG X7 and Varian 810MS). Analytical precision on the measured concentrations amount was less than 5%. Dedicated U uptake experiments for XPS, SEM and μRaman observations were performed at higher U concentration, i.e., 2×10^{-3} mol L^{-1} at three distinct pH (i.e., 3, 4 and 5.5). This concentration is above the schoepite solubility. However, a test experiment without pyrite during the same reaction time indicated the absence of any U phase precipitation.

2.6. Modelling

Sorption results were modelled using the Langmuir formalism. In this formalism, the cation is assumed to adsorb to a single site and the amount of sorbed cation or surface coverage Γ equals

$$\Gamma = \Gamma_{max} \frac{K_{ads}[cation]_{aq}}{1 + K_{ads}[cation]_{aq}} \quad (2)$$

where Γ_{max} is the saturation concentration per unit mass of pyrite (or site concentration), $[cation]_{aq}$ the aqueous concentration at equilibrium and K_{ads} the adsorption constant. Sorption isotherms can be described by three different domains according to the isotherm shape (Fig. 1). At low Γ, the isotherm displays a slope equal to one (domain 1). At higher Γ, the saturation is observed (domain 2). Last, domain 3 departs from sorption to a single site corresponds to the precipitation of a cation-bearing solid phase.

3. RESULTS

3.1. Pyrite characterization

3.1.1. Isoelectric point (pH_{IEP}) and point of zero charge (pH_{PZC})

Recorded zeta potentials for pyrite suspensions are all negative (Fig. 2). An isoelectric point pH_{PIE} of 1.90 could be extrapolated from the data. As $NaNO_3$ does not interact

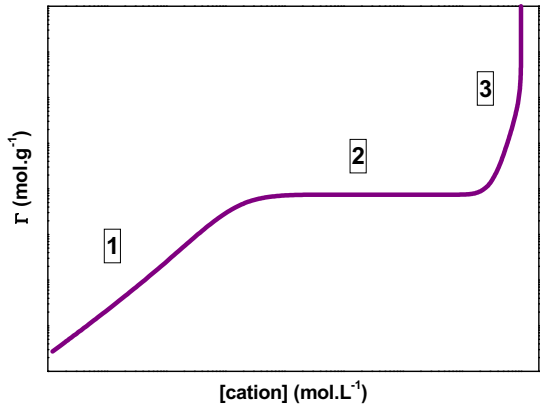

Fig. 1. Illustration of a concentration isotherm for one Langmuir sorption site and precipitation. Three different domains, namely 1, 2 and 3, can be distinguished. (1) Sorption on a Langmuir site. (2) Site saturation. (3) Solid precipitation.

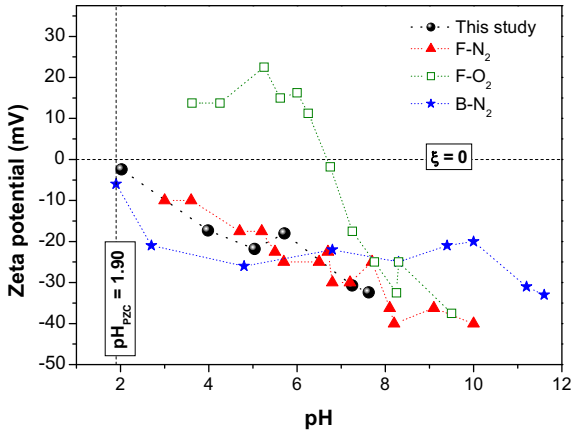

Fig. 2. Pyrite zeta potentials as a function of pH. F–N_2: data measured in N_2 atmosphere taken from Fornasiero et al. (1992); F–O_2: measured in O_2 atmosphere taken from Fornasiero et al. (1992); B–N_2: data measured in N_2 atmosphere taken from Bebié et al. (1998).

with pyrite surfaces, pH_{PIE} coincides with pH_{PZC}. Additional measurements performed with pyrite grains of smaller size (25–50 μm) led to the same pH_{PZC}. These results are consistent with previous published data obtained in N_2 atmosphere (Fornasiero et al., 1992; Bebié et al., 1998). Higher values were measured for oxidized pyrite (Fornasiero et al., 1992). Thus, it is clear that the pyrite surface is negatively charged at pH > 2, which should favour cation uptake.

3.1.2. Potentiometric titration

The surface site density calculated from the raw titration data equals 19 ± 3 sites nm^{-2}. However, this value should be corrected for the presence of dissolved Fe^{2+}, SO_4^{2-} and H^+ produced by the reaction of pyrite dissolution, according to

$$FeS_2 + 7/2O_2 + H_2O \rightarrow Fe^{2+} + 2SO_4^{2-} + H^+ \quad (3)$$

The $[Fe]_{aq}$ value was fixed at 4×10^{-6} mol L^{-1}, consistent with concentrations measured at pH 2. The corrected surface site density then equals $\Gamma_{max}(H^+) = 9 \pm 3$ sites nm^{-2}, confirming proton retention at the surface. This result is in good agreement with the surface site density reported by Weerasooriya and Tobschall (2005) from potentiometric titration, i.e., 11.96 ± 0.23 sites nm^{-2}.

3.1.3. Pyrite behaviour in solution

In every blank experiment, aqueous Fe was detected as $Fe^{(II)}$ only, while aqueous S was detected as sulphoxyanions such as $S_2O_3^{2-}$, $S_4O_6^{2-}$, SO_3^{2-} and SO_4^{2-}. This is consistent with previous observations (e.g., Goldhaber, 1983; Descostes et al., 2002). Note that $[Fe]_{aq}$ and $[S]_{aq}$ vary from one experiment to another and therefore cannot be directly compared. These discrepancies may reflect differences of reactivity of each natural pyrite sample (Cruz et al., 2001; Abraitis et al., 2004).

The surface of pristine FeS_2 was characterized by XPS and found to be free of any oxidation products. However,

when compared to pristine FeS_2, Fe-2p spectra obtained for the pyrite surface after hydration exhibits one additional peak at 708.7 eV which is consistent with a $Fe^{(II)}$–O bond (Fig. 3). As proposed below, this peak is attributed to a $Fe^{(II)}$ sorbed at the pyrite surface. No additional peak was observed on the S-2p spectra.

3.2. Cation uptake

3.2.1. Sorption of $Fe^{(II)}$ and $Co^{(II)}$

A slight sorption of ^{55}Fe is observed on pyrite, with a maximum of 22% of ^{55}Fe sorbed at pH 5 (Fig. 4). This demonstrates that Fe adsorbs on the pyrite surface, albeit this sorption would appear to be limited at first. Note, however, that stable Fe dissolved from pyrite was already present in the suspension (and probably sorbed as well), and so the added ^{55}Fe was isotopically diluted in this stable Fe pool. Thus, the actual amount of sorbed Fe may be estimated from this isotopic dilution, from $[Fe]_{aq}$, and from the fraction of sorbed ^{55}Fe, yielding an estimate of $\sim 10^{-6}$ mol L^{-1} at pH as low as 3. However, sorption data for ^{55}Fe show some scatter, which can be explained by various $[Fe]_{aq}$ resulting from pyrite dissolution. In contrast to Fe, uptake of Co strongly increases with a maximum at pH 5.5. The maximum $[Co]_{sorb}$ is $\sim 2 \times 10^{-6}$ mol L^{-1}, i.e., 3×10^{-7} mol g^{-1}. This indicates that $Co^{(II)}$ competes well with $Fe^{(II)}$ for sorption sites. Note that $Co^{(II)}$ uptake does not lead to significant drifts in pH.

3.2.2. Sorption of Eu and U

As observed for $Co^{(II)}$, uptake of $Eu^{(III)}$ is observed with a maximum at pH 5.5 (Fig. 4A), where nearly 100% of $Co^{(II)}$ and $Eu^{(III)}$ are sorbed. The same behaviour is observed for U (Fig. 4B) and is consistent with previous work (Wersin et al., 1994). However, the pH edge is steeper for $U^{(VI)}$. Moreover, at pH > 7, $U^{(VI)}$ sorption seems to slightly decrease with pH. This is consistent with a change of $U^{(VI)}$ speciation, i.e., the formation of dissolved anionic species such as $UO_2(OH)_3^-$, $UO_2(CO_3)_2^{2-}$, $(UO_2)_2(OH)_3CO_3^-$ and $UO_2(CO_3)_3^{4-}$. As mentioned previously, no significant pH drifts were observed at the end of reaction times.

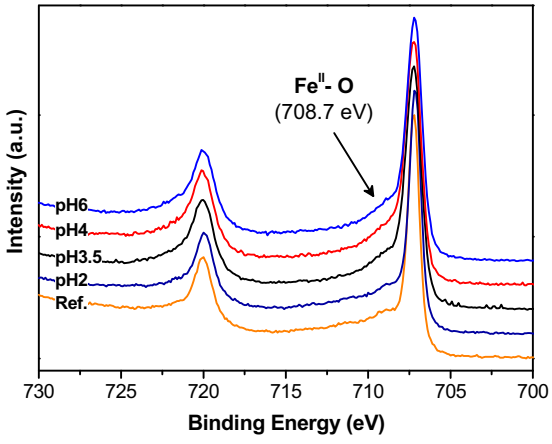

Fig. 3. Photoelectron spectra of Fe-2p lines of pyrite pristine surface and after hydration at different pH.

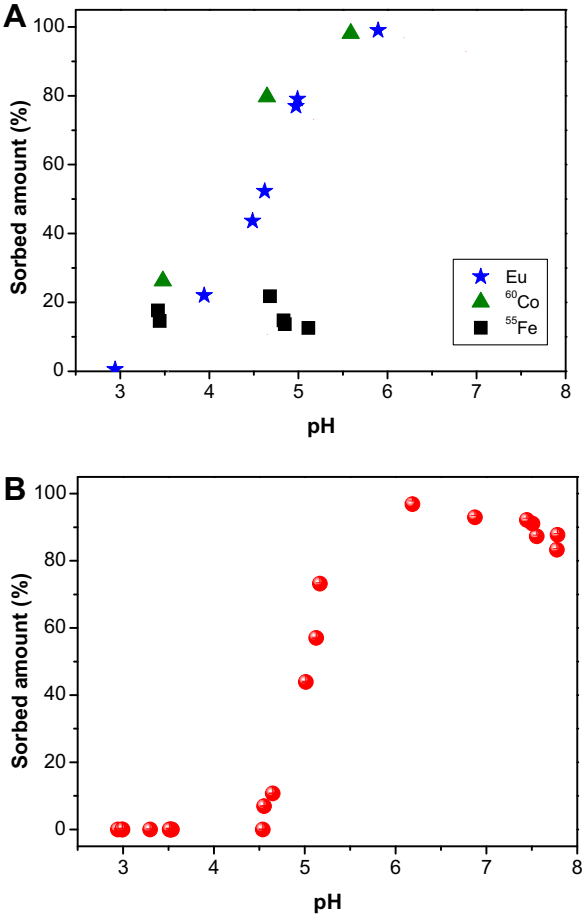

Fig. 4. (a) Sorption isotherm as a function of pH for $Eu^{(III)}$, $Co^{(II)}$ and $Fe^{(II)}$. (b) Sorption isotherm as a function of pH for $U^{(VI)}$. Chemical conditions are 8 g L^{-1} pyrite, 10^{-2} mol L^{-1} $NaNO_3$, $t = 48$ h. Uncertainty bars are masked by the points.

Isotherms of $Eu^{(III)}$ sorption as a function of $[Eu]_{aq}$ at pH 5.5 show two distinct parts (Fig. 5). At $[Eu]_{aq} \leqslant 10^{-7}$ mol g^{-1}, $[Eu]_{sorb}$ increases linearly with $[Eu]_{aq}$. At higher $[Eu]_{aq}$, a sorption plateau is reached, and apparent saturation is observed with $[Eu]_{sorb} \cong 1.25 \times 10^{-6}$ mol g^{-1}. A slightly different behaviour is observed for $U^{(VI)}$. At very low $[U]_{aq}$ up to $[U]_{sorb} = 10^{-9}$ M, the isotherm slope is nearly vertical. Afterwards, a linear relation with a slope comparable to that for $Eu^{(III)}$ is observed, up to $[U]_{aq} = 10^{-8}$ M. Finally, a sorption plateau corresponding to a maximum of $[U]_{sorb} \sim 5x10^{-8}$ mol g^{-1} is observed.

Isotherms of $Eu^{(III)}$ and $U^{(VI)}$ sorption were modelled using the Langmuir formalism (Fig. 5). For $U^{(VI)}$, this modelling was restricted to $[U]_{sorb} \geqslant 4 \times 10^{-9}$ mol g^{-1}, as a slope higher than 1 was observed for lower $[U]_{sorb}$. These modelling resulted in contrasted Γ_{max} and K_{ads} values (Table 1). In fact, even though Γ_{max} is smaller for $U^{(VI)}$ than for $Eu^{(III)}$, K_{ads} for $U^{(VI)}$ is greater than for $Eu^{(III)}$, suggesting a preferential sorption of the actinide. Yet, this simple Langmuir formalism fails to explain the relationship between $[U]_{sorb}$ and $[U]_{aq}$ at very low concentrations. In fact, the only way to interpret the experimental trend at low $[U]_{aq}$ is to consider the precipitation of a U-bearing

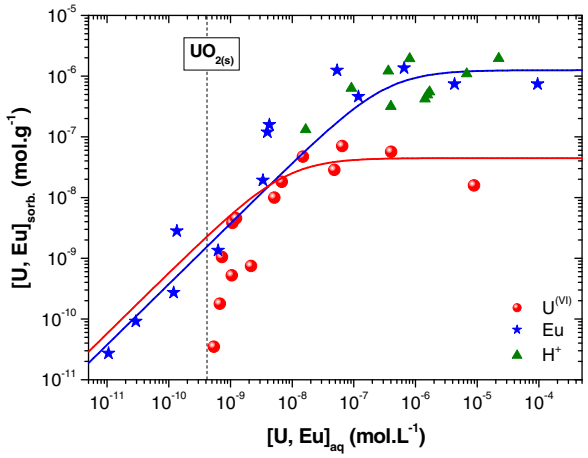

Fig. 5. Sorption isotherms of Eu and U on pyrite (8 g L^{-1}, $[NaNO_3] = 10^{-2}$ mol L^{-1}, pH 5.5, $t = 48$ h). Modelling according to the Langmuir formalism is conjointly plotted. Uncertainty bars are masked by the points. Additional data for H^+ sorption are taken from this study and Kamei and Ohmoto (2000).

Table 1
Results of modelling concentration isotherms according to the Langmuir formalism.

	U	Eu
Γ_{max} (mol g^{-1})	4.5×10^{-8}	1.25×10^{-6}
K_{ads} (L mol^{-1})	1.3×10^{8}	3×10^{6}

phase. In the experimental conditions, the solubility of $U^{(VI)}$ is higher than 10^{-4} mol L^{-1}. However, this solubility decreases down to $10^{-9.5}$ mol L^{-1} if $U^{(IV)}$ is considered, i.e., if the formation of UO_2(s) is postulated. Such a value is very close to the experimentally observed $[U]_{aq}$ (Fig. 5). Thus the steep slope observed at low $[U]_{aq.}$ is interpreted as a reduction of $U^{(VI)}$ onto the pyrite surface. Microscopic and spectroscopic techniques were used to assess the reality of such a reduction reaction.

3.3. Uranium reduction observed by surface characterization techniques

Images of the pyrite surface by SEM in BackScattered Electron (BSE) mode revealed the presence of very bright (electron dense) spots (Fig. 6). These spots seem to be preferentially located on the structural defaults of the pyrite surface, such as grain edges or craters. These spots were shown by EDS to be made essentially of U and O (Fig. 7). This U local concentration on structural defaults of the pyrite surface conforms to previous descriptions reported by Wersin et al. (1994) and Scott et al. (2007), and parallels Pd results (Hyland and Bancroft, 1990).

Complementary XPS characterizations were performed on the same samples reacted at pH 6.1, close to the maximum $U^{(VI)}$ uptake (Figs. 8 and 9). The U-4f peaks were decomposed first by scaling the reference spectrum of $UO_2(OH)_2$(s) to the sample spectrum (Fig. 9a). The sample spectrum could not be modelled by this single contribution, and an additional component at 380.5 eV had to be added.

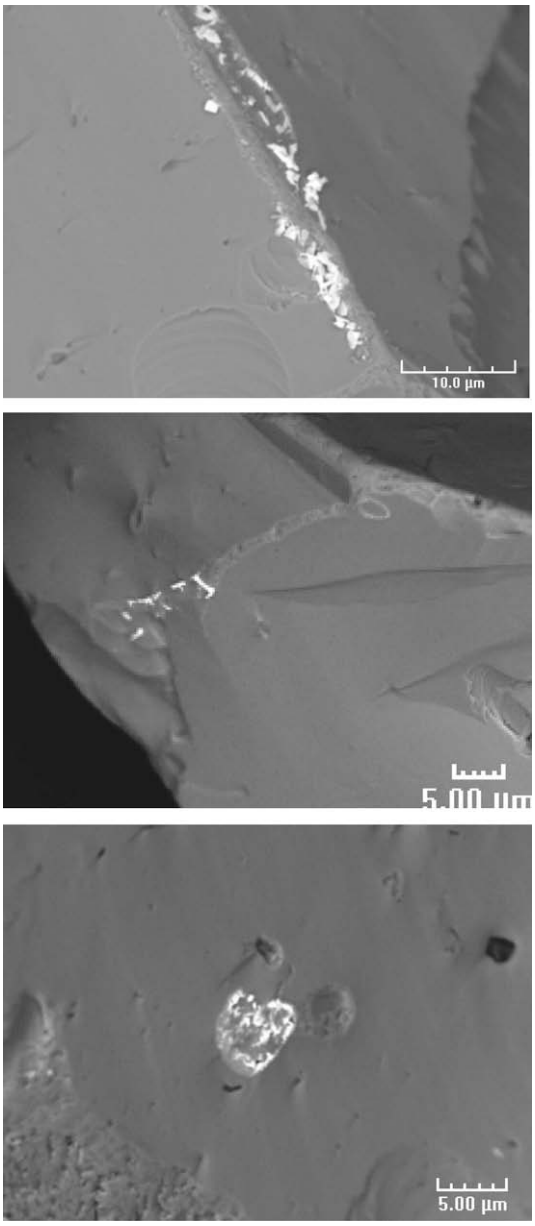

Fig. 6. Backscattered Electron images of the pyrite surface in the presence of U (pH 5.5, $[U]_{tot} = 2 \times 10^{-3}$ mol L^{-1}).

This contribution at 380.5 eV is consistent with reduced U (Chadwick, 1973; Allen et al., 1974; Wersin et al., 1994), but its weak amplitude precludes detection of a corresponding satellite. The absence of photoreduction was tested as the intensity of the peak observed at 380.5 eV remained constant during the whole acquisition duration.

When compared to pristine FeS_2, Fe-2p spectra obtained for the U-reacted pyrite surface exhibit two additional peaks at 708.2 and 711.1 eV, respectively (Fig. 9b). These peaks are consistent with a $Fe^{(II)}$–O bond or $Fe^{(II)}$ sorbed at the pyrite surface, and a $Fe^{(III)}$–O environment, respectively. When compared to pristine pyrite, the S-2p spectra exhibit two additional components at 164.8 and 165.8 eV (Fig. 9c). They are attributed to oxidized S at an oxidation state lower than +2 (see Fig. 10).

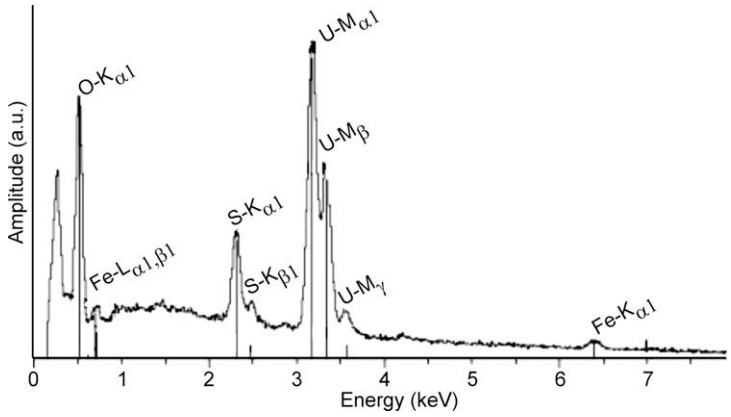

Fig. 7. Energy dispersive X-ray spectra of the U enriched zone observed on the pyrite surface (pH 5.5, $[U]_{tot} = 2 \times 10^{-3}$ mol L^{-1}).

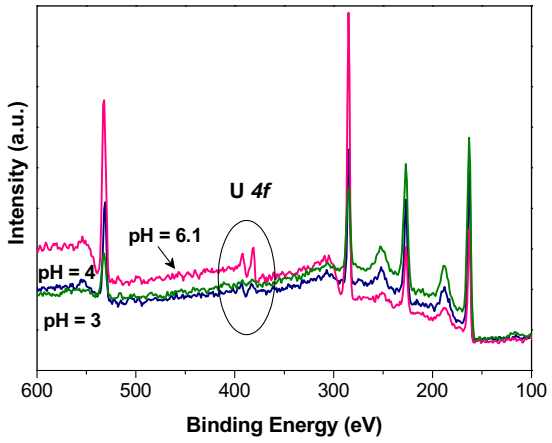

Fig. 8. Photoelectron survey spectra of pyrite surface in the presence of U at pH 3, 4 and 6.1 ($[U]_{tot} = 2 \times 10^{-3}$ mol L^{-1}).

Complementary characterization of the pyrite surface was performed by μRaman spectroscopy (Fig. 11). Disulphide phonons from FeS_2 at 342, 378 and 429 cm^{-1} were observed (Toniazzo et al., 1999; McGuire et al., 2001). An additional peak is observed at 629 cm^{-1} on several dark areas of the pyrite sample reacted with $U^{(VI)}$ and therefore cannot be attributed to an artefact from grain orientation. This band is consistent with the deformation of the O–S–O bond observed with $S_2O_3^{2-}$ (Rintoul et al., 1997). However, the absence of any additional band does not allow a complete identification of this sulphoxyanion. Last, no $U^{(VI)}$ characteristic band is observed, although uranyl is known to exhibit a main peak at 870 cm^{-1} (Dai et al., 1996) whereas reduced UO_{2+x} is characterized by bands located at 450, 750 and 1150 cm^{-1} (Manara and Renker, 2003).

4. DISCUSSION

4.1. Density of surface sites and implications for the nature of predominant sites

Some insight into the nature of the predominant sites at the pyrite surface may be gained from potentiometric titration and electrophoresis. The low pH_{PZC} suggests that sulphide groups, not Fe-bound hydroxyls, control then surface charge (Sun et al., 1991; Dekkers and Schoonen, 1994; Vaughan et al., 1997; Bebié et al., 1998; Guevremont et al., 1998; Rosso et al., 1999). This assumption is supported by the S-enrichment observed for pyrite surfaces for all common {1 0 0}, {1 0 1} and {1 1 1} crystallographic orientations (Elestinov et al., 2000). The total amount of surface sites may be further estimated from the specific surface area and from the density of surface sites which is itself governed by the surface crystallographic orientation and the mineral bulk structure. Even if it is known that surfaces obtained by pyrite cleaving appear conchoidal, fracture propagation is guided at the microscopic scale by {1 0 0} planes (Eggleston and Hochella, 1992; Rosso et al., 1999). Therefore, the {1 0 0} plane can be considered as predominant. On this surface, two Fe and two S are exposed per surface unit cell (5.41×5.41 $Å^2$). Surface occupancy by Fe and S atoms can be further calculated in a first approximation from their ionic radii ($S^{(-II)}$: 1.84 Å; $Fe^{(II)}$: 0.74 Å; Shannon, 1976). Hence, the surface percentage covered by S atoms equals $2 \times \pi \times (1.84 \times 10^{-10})^2/(5.41 \times 10^{-10})^2 = 73\%$.

Pyrite surface charge can be governed by protonation–deprotonation reactions of the surface S groups (noted ≡S) according to

$$\equiv S - H \leftrightarrows \equiv S^- + H^+ \quad (4)$$

During surface hydration, water decomposition can occur either at S sites, leading to hydroxyl release, or at Fe sites, leading to a release of protons in solution (Weerasooriya and Tobschall, 2005):

$$\equiv S^- + H_2O \leftrightarrows \equiv S - H + OH^- \quad (5)$$

$$\equiv Fe^+ + H_2O \leftrightarrows \equiv Fe - OH + H^+ \quad (6)$$

where $\equiv S^-$ and $\equiv Fe^+$ are surface exposed S and Fe, the charges of which are partially neutralized by structural atoms. Hence the pH increase observed during the first dissolution experiments, but also in oxic media in the first minutes (Kamei and Ohmoto, 2000; Descostes et al., 2004) can be explained by the predominance of reaction (5) over (6). This is in line with the greater proportion of mineral surface covered by ≡S groups, but may also be explained by a greater chemical affinity for (5) than for (6).

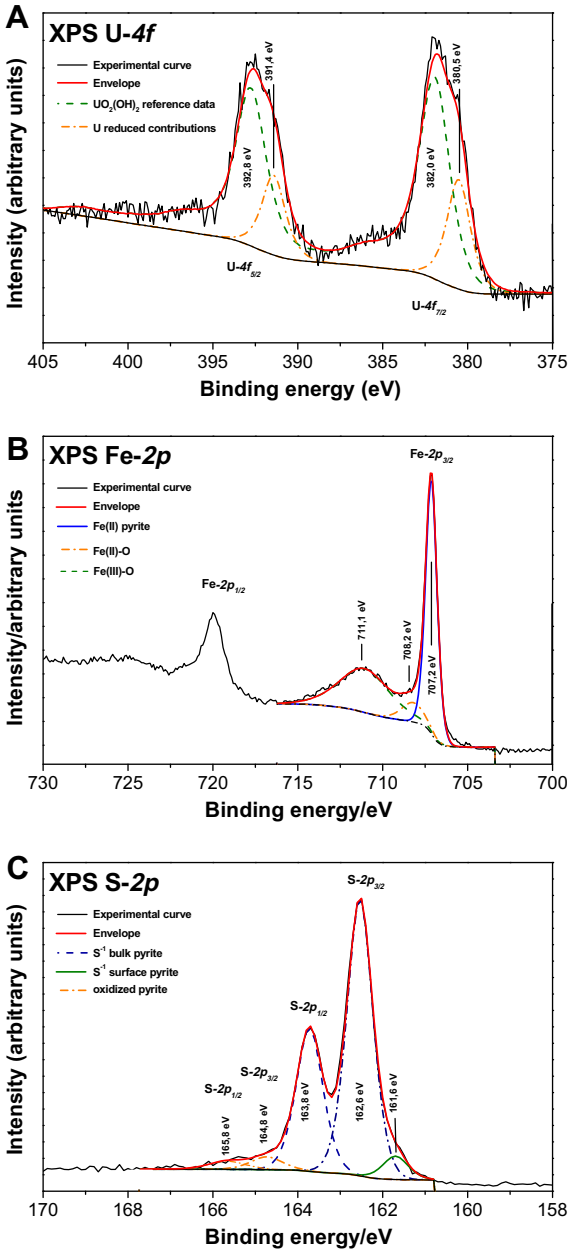

Fig. 9. Photoelectron spectra of U-4f (A), Fe-2p (B) and S-2p (C) lines of the pyrite surface in the presence of U at pH 6.1 ($[U]_{tot} = 2 \times 10^{-3}$ mol L^{-1}).

The surface site density corrected from potentiometric titrations, i.e., 9 ± 3 sites nm^{-2}, can be compared to that estimated from crystallographic considerations. The {1 0 0} surface cell has an area of 2.93×10^{-19} m^2 and displays two S atoms; hence the surface density of S atoms equals 6.8 sites nm^{-2}, comparable to the value obtained from direct titration. For an 8 g L^{-1} suspension of pyrite with a specific surface area of 0.06 m^2 g^{-1}, this leads to an amount of proton sites of 7.1 ± 3 μmol L^{-1} (from titration data), and of ≡S surface sites of 5.4 μmol L^{-1} (from crystallographic titration data). These values compare well with the maximal amount of cation sorbed in our experiments, and suggest that S sites can account for both surface protonation and cation sorption.

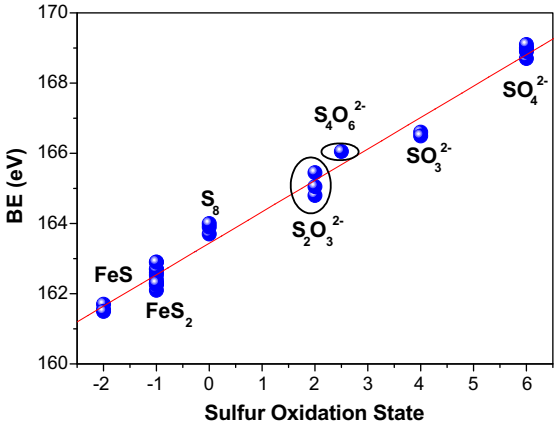

Fig. 10. Evolution of BE (in eV) of the $S2p_{3/2}$ photoelectron peak in function of the oxidation state of S. Modified from Descostes et al. (2006).

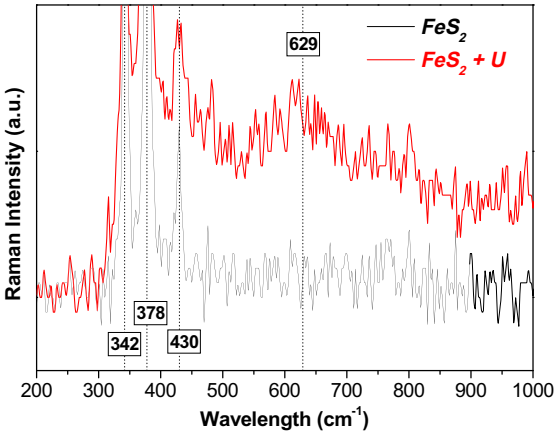

Fig. 11. Comparison of Raman spectra of unreacted pyrite and pyrite reacted with U (pH 5.5, $[U]_{tot} = 2 \times 10^{-3}$ mol L^{-1}).

4.2. Iron sorption and surface protonation

Iron (II) uptake cannot be explained by the precipitation of $Fe^{(II)}$ minerals since the concentrations measured in our experimental conditions are below the solubility of any $Fe^{(II)}$ phase. Iron (II) uptake therefore results from sorption onto the surface pyrite. This is consistent with the detection of $Fe^{(II)}$–O bond at 708.7 eV and is supported by previous studies of divalent cation uptake by pyrite (Jean and Bancroft, 1986; Kornicker and Morse, 1991; Ehrhardt et al., 2000).

Sorption of $Fe^{(II)}$ was previously and indirectly reported by Descostes et al. (2004). These authors studied the oxidative dissolution of pyrite in acidic media (pH ⩽ 3). In the first stages, a systematic deficit in aqueous $Fe^{(II)}$ was observed leading to $R = [S]_{tot}/[Fe]_{tot}$ higher than 2. Values taken from this study are plotted in Fig. 12. Additional data obtained in anoxia at pH 2 in $HClO_4$ media in the same experimental conditions (run M06 in Descostes et al.,

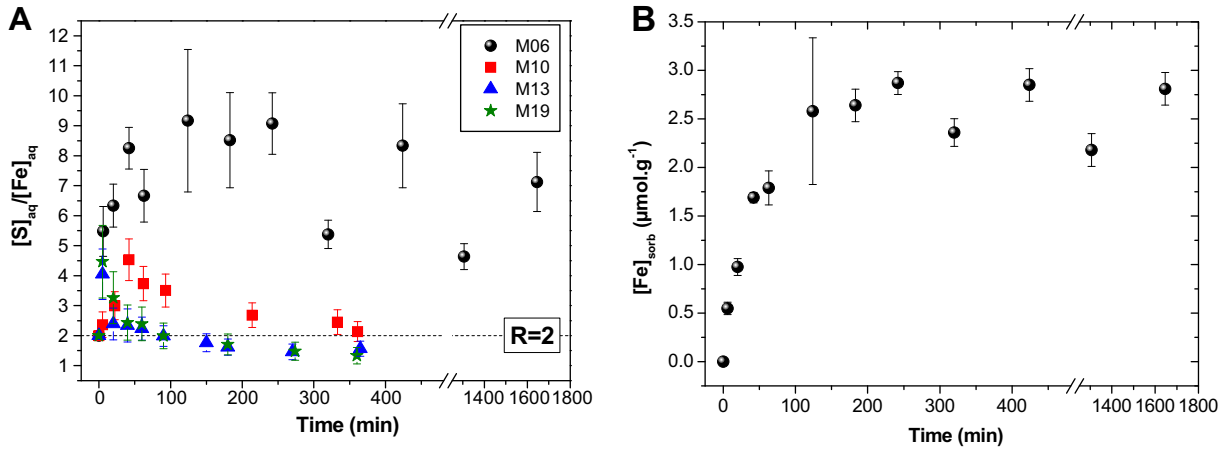

Fig. 12. (A) Evolution of $R = [S]_{aq}/[Fe]_{aq}$ as a function of time indicating $Fe^{(II)}$ sorption onto pyrite. (B) Estimation of $[Fe]_{sorb}$ as a function of time observed in run M06 (B). Data taken from Descostes et al. (2004).

2004, and additional data at $t > 24$ h for this run) all yield $R > 2$ even for experiments longer than 24 h. From this last experiment, it is also possible to calculate a maximum $[Fe]_{sorb}$ assuming stoichiometric dissolution of pyrite and S complete oxidation, leading to

$$[Fe]_{sorb} = 0.5[SO_4^{2-}]_{aq} - [Fe]_{aq} \quad (7)$$

The $[Fe]_{sorb}$ values are plotted in Fig. 11 and indicate a maximum $[Fe]_{sorb} = 17.5 \times 10^{-6}$ mol L^{-1} (2.5×10^{-6} mol g^{-1}). This value is somewhat higher than the maximal amount of sorbed cation in our study (1.25×10^{-6} mol g^{-1}). The difference may result from the difference in pH between the studies of Descostes et al. (2004) (pH. 2.5) and the present one (pH 5.5). Note that such deficit in dissolved Fe was also reported by Moses and Herman (1991). Weerasooriya and Tobschall (2005) also reported Fe sorption with $\Gamma_{max} = 10^{-5}$ mol g^{-1} in a pH range between 2 and 6.

Proton sorption has been observed in this and other studies (Kamei and Ohmoto, 2000). The pH dependence of surface protonation as a function of pH can be rationalized by a sorption isotherm, as for any sorbate. Selected data were obtained between pH 4.7 and pH 7.7, and corrected for the presence of Fe^{2+}, SO_4^{2-} and H^+ produced by the pyrite dissolution. Calculated data are plotted conjointly with $Eu^{(III)}$ and $U^{(VI)}$ in Fig. 5. Overall, the sorption isotherm for $Eu^{(III)}$ and protons are close to one another, suggesting similar, if not identical, sorption sites.

4.3. Sorption of Eu and U

4.3.1. Existence of distinct sorption sites

Because $Fe^{(II)}$ and protons can sorb onto the pyrite surface, they may compete with $Eu^{(III)}$ and $U^{(VI)}$ for sorption sites. Unfortunately, it was not possible to quantify the amount of sorbed or desorbed $Fe^{(II)}$ during $U^{(VI)}$ and $Eu^{(III)}$ sorption experiments as the expected variations in $[Fe]_{aq}$ are too low, i.e., between 10^{-10} and 10^{-6} mol L^{-1}. These small amounts are masked by $Fe^{(II)}$ released by conventional dissolution. Therefore, we can neither prove nor exclude a cationic exchange between $Fe^{(II)}$ and $U^{(VI)}$ or $Eu^{(III)}$ on sorption sites.

The discrepancies in K_{ads} and Γ_{max} for $Eu^{(III)}$ and $U^{(VI)}$ can be explained by the existence of distinct sorption sites. On the one hand, a simple sorption site, namely S1 with a $\Gamma_{max} = 1.25 \times 10^{-6}$ mol g^{-1} can completely explain $Eu^{(III)}$ sorption whatever the cation concentration. Considering the specific surface area of pyrite in this study, the maximum density of sorbed $Eu^{(III)}$ equals ~12 Eu atoms nm^{-2}. This value is rather high, but consistent with the site density calculated by potentiometric titration, i.e., 9 ± 3 sites nm^{-2}. Hence $Eu^{(III)}$ may sorb on protonated sites. On the other hand, $U^{(VI)}$ isotherm exhibits a unique shape characterized by a steep increase in $[U]_{sorb}$ at low $[U]_{aq}$, and then a Langmuir-like sorption behaviour suggesting sorption on a single site. Yet, if this site were active over the entire $[U]_{aq}$, it would have led to an $[U]_{sorb}$ higher than observed at low $[U]_{aq}$. To overcome this difficulty, the simplest hypothesis is to assume that this site was somewhat "activated" by $U^{(VI)}$ sorption and reduction at low $[U]_{aq}$. Furthermore, spectroscopic results clearly demonstrate that part, but not all, of sorbed $U^{(VI)}$ is reduced, and $[U]_{aq}$ observed for the steep part of the isotherm compares well with the solubility of $UO_2(s)$, i.e., $10^{-9.5}$ mol L^{-1}. All these results can be rationalized in a conceptual model. The model assumes that $U^{(VI)}$ would be first sorbed on a "reducing" site S2 with a maximal capacity of about 5×10^{-9} mol g^{-1}, and resulting in the reduction of sorbed $U^{(VI)}$. This reducing capacity would be limited to the defect zones where precipitation of $U^{(VI)}$ was observed. These defect sites are thought to be the primary location for U reduction, as previously observed for sorption and reduction of $Au^{(III)}$ onto the pyrite surface (Mycroft et al., 1995). Indeed, defects sites are highly reactive (Bostick et al., 2000), and can act as high energy sites where a sorbed molecule would be easily reduced, or as preferential nucleation sites for new particles (Hyland and Bancroft, 1990).

Once the S2 site is saturated, a new site S3 is activated according to a change in the electronic properties of the pyrite surface. This site exhibits a higher retention capacity with $\Gamma_{max} = 4.5 \times 10^{-8}$ mol g^{-1}, lower than Γ_{max} for Eu S1 sites. It may be possible that S3 is a subset of S1. The lower Γ_{max} for $U^{(VI)}$ would then be explained by the higher size of UO_2^{2+}, which would mask the neighbouring sites. In con-

trast, $Eu^{(III)}$ ion with its smaller ionic radius, would access to all the sorption sites. However, the change in reactivity of these sites upon $U^{(VI)}$ sorption at low $[U]_{aq}$ would need further investigation.

Difference in the affinity of $U^{(VI)}$ and $Eu^{(III)}$ for the pyrite surface could be explained by the Hard and Soft Acid and Base (HSAB) theory, as proposed by Moses and Herman (1991) to explain preferential sorption of $Fe^{(II)}$ over $Fe^{(III)}$ on pyrite. Initially, this theory was developed and applied to the formation of aqueous species, but can be extended to interfacial reactions. According to the HSAB theory, a soft acid (e.g., $U^{(VI)}$), would have a higher affinity than a harder acid (as $Eu^{(III)}$) towards a soft base (e.g., a S atom forming a ≡S surface group, where ≡ stands for the solid). Hence, the chemical bond ≡S–$U^{(VI)}$ would exhibit a more pronounced covalent character than the ≡S–$Eu^{(III)}$ bond. Moreover, the O atoms from the $U^{(VI)}$ oxo motif can form hydrogen bonds with ≡SH groups from the pyrite surface, which would stabilize ≡S–$U^{(VI)}$ surface complexes. This would not be the case for $Eu^{(III)}$, thus explaining the lower constant K_{ads} modelled for $Eu^{(III)}$.

4.3.2. Uranium reduction

Spectroscopic data confirmed the presence of reduced U at the pyrite surface, probably as a mixed $U^{(VI)}$–$U^{(IV)}$ oxide, noted $UO_{2+x}(s)$. If the total U concentration sorbed at the pyrite surface and observed by XPS is fixed at 4.5×10^{-8} mol g^{-1}, i.e., $\Gamma_{max}(U^{(VI)})$, then the fraction of reduced U measured by XPS allows to calculate a reduced U concentration of 5×10^{-9} mol g^{-1}. Such a value is consistent with the maximum capacity of the "reducing" site S2. Reduction of U would occur at the pyrite surface, after sorption of $U^{(VI)}$. Such a reaction pathway was already proposed by Wersin et al. (1994), by Hyland and Bancroft (1990) to explain the reduction of $Pd^{(II)}$ into $Pd^{(0)}$ at the pyrite surface, and by Rimstidt and Vaughan (2003) to model pyrite oxidation by $Fe^{(III)}$. Reduction of $U^{(VI)}$ would be paralleled by the oxidation of S to form either elementary $S^{(0)}$ or—subsequently—sulphoxyanions. Note that $S^{(0)}$ was not detected by XPS, but this may simply result from the high volatility of $S^{(0)}$, which tends to sublimate in vacuum even at 270 K (Mycroft et al., 1990). As far as μRaman spectroscopy is concerned, $S^{(0)}$ bands at 436 and 472 cm^{-1} are very close to the ones of FeS_2 disulphide phonons at 429 cm^{-1}, precluding discrimination of these species. An additional Raman band was observed at 629 cm^{-1} and is consistent with S–O bonds. Also, Raman spectroscopy probes a sample depth not shallower than a few nm, too insensitive to distinguish a monoatomic layer of $S^{(0)}$ from the pyrite bulk signature.

Based on these observations, and on the hypothesis of $S^{(0)}$ formation, the overall reaction of $U^{(VI)}$ reduction and S oxidation can be written:

$$(1-x)FeS_2 + UO_2^{2+} + xH_2O \rightarrow (1-x)Fe^{2+} + 2(1-x)S^0 + UO_{2+x}(s) + 2xH^+ \quad (8)$$

According to the value of x, $\Delta_R G$ can be calculated (see Table 2). Formation of hyperstoichiometric UO_{2+x} such as $U_4O_9(s)$, $U_3O_7(s)$ and to a less extent $UO_2(s)$ seems to be favoured even if $U_3O_8(s)$ was proposed as the U reduced phase (Wersin et al., 1994; Aubriet et al., 2006).

Table 2
Calculated Gibbs free energy of reaction ($\Delta_R G$) for uranium reduction (Eq. (8)) as a function of $UO_{2+x}(s)$ stoichiometry.

	$UO_2(s)$	$U_4O_9(s)$	$U_3O_7(s)$	$U_3O_8(s)$
U oxidation number	4	4.5	4.67	5.33
$\Delta_R G^0$ (kJ mol^{-1})	−13.64	−32.26	−15.73	28.09

5. CONCLUSIONS

This study confirms that pyrite is an efficient scavenger of $Fe^{(II)}$, $Co^{(II)}$, $Eu^{(III)}$ and $U^{(VI)}$ cations for an extended range of pH, with a sorption maximum at pH 5.5. Retention of $Fe^{(II)}$ at the pyrite surface provides a rationale for non-stoichiometric $[S]_{tot}/[Fe]_{tot}$ observed during pyrite dissolution. Sorption of $Eu^{(III)}$ could be explained by the existence of a unique sorption site according to the Langmuir formalism. In the case of $U^{(VI)}$, a more complex uptake behaviour is observed. At low concentration, adsorbed $U^{(VI)}$ is reduced and probably precipitates as hyperstoichiometric UO_{2+x}, while S is oxidized. This redox process seems to be limited to a few sites as $U^{(VI)}$ reduction is less efficient at higher concentrations. Reduction of $U^{(VI)}$ is proposed to occur on defect sites.

These results highlight the role played by pyrite on the mobility of cations in natural environments, not only in terms of reductive immobilization, but also for simple sorption, even for redox-sensitive elements. Hence several sorption mechanisms can operate, leading to contrasted impacts in terms of sorption reversibility. Thus, these sulphide solids can potentially control the transfer of cations in the natural environment, especially in the water–sediment interface where anoxic conditions prevail. In addition, competition between cations for the sorption sites may potentially thwart the uptake and reduction of species with little affinity for the pyrite surface. In contrast, cation retention under near-neutral pH conditions may alter the pyrite surface charge and somewhat favour interaction of simple or electroactive anions with the surface. Future studies are needed to assess the importance of such cooperative retention.

ACKNOWLEDGMENTS

The authors would like to thank D. Stammose and A. Mifsud from the Laboratoire d'Etude des Transferts dans les Sols (IRSN) for the uranium analysis, J.L. Lacour, C. Blanc, M. Tabarant and A. Chenière from the Laboratory for the Reactivity of Surfaces and Interfaces for their assistance in respectively μRaman spectroscopy, SEM, ICP-AES and XRD characterization. We also would like to thank Prof. D. Vaughan and three anonymous reviewers for their fruitful suggestions to improve this article.

REFERENCES

Abraitis P. K., Pattrick R. A. D. and Vaughan D. J. (2004) Variations in the compositional, textural and electrical properties of natural pyrite: a review. *Int. J. Miner. Process.* **74**, 41–59.

Allen G. C., Crofts J. A., Curtis M. T. and Tucker P. M. (1974) X-ray photoelectron spectroscopy of some uranium oxide phases. *J. Chem. Soc., Dalton Trans.* **12**, 1296–1301.

ANDRA, 2005. *Evaluation de la faisabilité du stockage géologique en formation argileuse*. Andra, Chatenay-Malabry, France.

Aubriet H., Humbert B. and Perdicakis M. (2006) Interaction of U(VI) with pyrite, galena and their mixtures: a theoretical and multitechnique approach. *Radiochim. Acta* **94**, 657–663.

Beaucaire C., Pitsch H., Toulhoat P., Motellier S. and Louvat D. (2000) Regional fluid characterisation and modelling of water–rock equilibria in the Boom clay Formation and in the Rupelian aquifer at Mol, Belgium. *Appl. Geochem.* **15**, 667–686.

Beaucaire C., Michelot J.-L., Savoye S. and Cabrera J. (2008) Groundwater characterisation and modelling of water–rock interaction in an argillaceous formation (Tournemire, France). *Appl. Geochem.* **23**, 2182–2197.

Bebié J., Schoonen M. A. A., Fuhrmann M. and Strongin D. R. (1998) Surface charge development on transition metal sulfides: an electrokinetic study. *Geochim. Cosmochim. Acta* **62**, 633–642.

Bostick B. C., Fendorf S. and Fendorf M. (2000) Disulfide disproportionation and CdS formation upon cadmium sorption on FeS_2. *Geochim. Cosmochim. Acta* **64**, 247–255.

Chadwick D. (1973) Uranium 4f binding energies studied by X-ray photoelectron spectroscopy. *Chem. Phys. Lett.* **21**, 291–294.

Cruz R., Bertrand V., Monroy M. and Gonzalez I. (2001) Effect of sulfide impurities on the reactivity of pyrite and pyritic concentrates: a multi-tool approach. *Appl. Geochem.* **16**, 803–819.

Dai S., Lee Y.-H. and Young J. P. (1996) Observation of the surface-enhanced scattering spectrum of uranyl ion. *Appl. Spectrosc.* **50**, 536–537.

Dekkers M. J. and Schoonen M. A. A. (1994) An electrokinetic study of synthetic greigite and pyrrhotite. *Geochim. Cosmochim. Acta* **58**, 4147–4153.

Descostes M., Mercier F., Thromat N., Beaucaire C. and Gautier-Soyer M. (2000) Use of XPS to the determination of chemical environment and oxidation state of iron and sulfur samples. Constitution of a data basis in binding energies for Fe and S reference compounds and applications to the evidence of surface species of an oxidized pyrite in a carbonate medium. *Appl. Surf. Sci.* **165**, 288–302.

Descostes M., Beaucaire C., Mercier F., Savoye S., Sow J. and Zuddas P. (2002) Effect of carbonate ions on pyrite (FeS_2) dissolution. *Bull. Soc. Geol. Fr.* **173**, 265–270.

Descostes M., Vitorge P. and Beaucaire C. (2004) Pyrite oxidation in acidic media. *Geochim. Cosmochim. Acta* **68**, 4559–4569.

Descostes M., Vitorge P. and Beaucaire C. (2006) Pyrite (FeS2) oxidation as a function of pH: a multitechnique approach. *Geochim. Cosmochim. Acta* **70**(18), A138.

Dodge C. J., Francis A., Gillow J. B., Halada G. P., Eng C. and Clayton C. R. (2002) Association of uranium with iron oxides typically formed on corroding steel surfaces. *Environ. Sci. Technol.* **36**, 3504–3511.

Dunn D. S., Bogart M. B., Brossia C. S. and Cragnolino G. A. (2000) Corrosion of iron under alternating wet and dry conditions. *Corros. Sci.* **56**, 470–481.

Eggleston C. M. and Hochella, Jr., M. F. (1992) Scanning tunneling microscopy of pyrite (1 0 0)—surface-structure and step reconstruction. *Am. Miner.* **77**, 221–224.

Eglizaud N. (2006) Rétention et réduction de l'uranium à la surface de la pyrite. Ph.D. thesis, Paris XI University.

Eglizaud N., Miserque F., Simoni E., Schlegel M. and Descostes M. (2006) Uranium(VI) interaction with pyrite (FeS_2): chemical and spectroscopic studies. *Radiochim. Acta* **94**, 651–656.

Ehrhardt J. J., Berha P., Bonnissel-Gissinger P. and Alnot M. (2000) XPS study of the sorption of Hg(II) onto pyrite FeS_2. *Surf. Interface Anal.* **30**, 269–272.

El Aamrani S., Giménez J., Rovira M., Seco F., Grivé M., Bruno J., Duro L. and de Pablo J. (2007) A spectroscopic study of uranium(VI) interaction with magnetite. *Appl. Surf. Sci.* **253**, 8794–8797.

Elestinov A. R., Guevremont J. M., Strongin D. R., Schoonen M. A. A. and Strongin M. (2000) Oxidation of 1 0 0 and 1 1 1 surfaces of pyrite: effects of preparation method. *Am. Miner.* **85**, 623–626.

Fornasiero D., Ejit V. and Ralston J. (1992) An electrokinetic study of pyrite oxidation. *Colloids Surf. A* **62**, 63–73.

Gabriel U., Gaudet J.-P., Spadini L. and Charlet L. (1998) Reactive transport of uranyl in a goethite column: an experimental and modelling study. *Chem. Geol.* **151**, 107–128.

Gaucher E. C., Blanc P., Bardot F., Braibant G., Buschaert S., Crouzet C., Gautier A., Girard J.-P., Jacquot E., Lassin A., Negrel G., Tournassat C., Vinsot A. and Altmann S. (2006) Modelling the porewater chemistry of the Callovian–Oxfordian formation at a regional scale. *C. R. Geosci.* **338**, 917–930.

Goldhaber M. B. (1983) Experimental study of metastable sulfur oxyanion formation during pyrite oxidation at pH 6–9 and 30 °C. *Am. J. Sci.* **283**, 193–217.

Grambow B., Smailos E., Geckeis H., Müller R. and Hentschel H. (1996) Sorption and reduction of uranium(VI) on iron corrosion products under reducing saline conditions. *Radiochim. Acta* **74**, 149–154.

Guevremont J. M., Strongin D. R. and Schoonen M. A. A. (1998) Thermal chemistry of H_2S and H_2O on the (1 0 0) plane of pyrite: unique reactivity of defect sites. *Am. Miner.* **83**, 1246–1255.

Guo Z., Li Y. and Wu W. (2009) Sorption of U(VI) on goethite: effects of pH, ionic strength, phosphate, carbonate and fulvic acid. *Appl. Radiat. Isot.* **67**, 996–1000.

Hsi C. D. and Langmuir D. (1985) Adsorption of uranyl onto ferric oxyhydroxides: application of the surface complexation site-binding model. *Geochim. Cosmochim. Acta* **49**, 1931–1941.

Hyland M. M. and Bancroft G. M. (1990) Palladium sorption and reduction on sulfide mineral surfaces—an XPS and AES study. *Geochim. Cosmochim. Acta* **54**, 117–130.

Hyland M. M., Jean G. E. and Bancroft G. M. (1990) XPS and AES studies of Hg(II) sorption and desorption reactions on sulphide minerals. *Geochim. Cosmochim. Acta* **54**, 1957–1967.

Jean G. E. and Bancroft G. M. (1986) Heavy metal adsorption by sulphide mineral surfaces. *Geochim. Cosmochim. Acta* **50**, 1455–1463.

Kamei G. and Ohmoto H. (2000) The kinetics of reactions between pyrite and O_2-bearing water revealed from in situ monitoring DO, Eh and pH in a closed system. *Geochim. Cosmochim. Acta* **64**, 2585–2601.

Kornicker W. A. and Morse J. W. (1991) Interactions of divalent cations with the surface of pyrite. *Geochim. Cosmochim. Acta* **55**, 2159–2171.

Lenhart J. J. and Honeyman B. D. (1999) Uranium(VI) sorption to hematite in the presence of humic acid. *Geochim. Cosmochim. Acta* **63**, 2891–2901.

Manara D. and Renker B. (2003) Raman spectra of stoichiometric and hyperstoichiometric uranium dioxide. *J. Nucl. Mater.* **321**, 233–237.

McGuire M. M., Jallad K. N., Ben-Amotz D. and Hamers R. J. (2001) Chemical mapping of elemental sulphur on pyrite and arsenopyrite surfaces using near-infrared Raman imaging spectroscopy. *Appl. Surf. Sci.* **178**, 105–115.

Missana T., Garcia-Guttierrez M. and Maffiotte C. (2003) Experimental and modelling study of the uranium (VI) sorption on goethite. *J. Colloid Interface Sci.* **260**, 291–301.

Moses C. O. and Herman J. S. (1991) Pyrite oxidation at circumneutral pH. *Geochim. Cosmochim. Acta* **55**, 471–482.

Murphy R. J., Lenhart J. J. and Honeyman B. D. (1999) The sorption of thorium (IV) and uranium (VI) to hematite in the

presence of natural organic matter. *Colloids Surf. A: Physicochem. Eng. Aspects* **157**, 47–62.

Mycroft J. R., McIntyre N. S., Lorimer J. W. and Hill I. R. (1990) Detection of sulfur and polysulphides on electrochemically oxidized pyrite surfaces by X-ray photoelectron spectroscopy and Raman spectroscopy. *J. Electroanal. Chem.* **292**, 139–152.

Mycroft J. R., Bancroft G. M., McIntyre N. S. and Lorimer J. W. (1995) Spontaneous deposition of gold on pyrite from solutions containing Au(III) and Au(I) chlorides: Part I. A surface study. *Geochim. Cosmochim. Acta* **59**, 3351–3365.

NAGRA (2002) Project Opalinus Clay: Safety Report—Demonstration of Disposal Feasibility for Spent Fuel, Vitrified High-Level Waste and Long-Lived Intermediate-Level Waste (Entsorgungsnachweis). NAGRA.

ONDRAF (2001) Technical Overview of the SAFIR 2 Report. ONDRAF.

Rimstidt J. D. and Vaughan D. J. (2003) Pyrite oxidation: a state-of-the-art assessment of the reaction mechanism. *Geochim. Cosmochim. Acta* **67**, 873–880.

Rintoul L., Crawford K., Shurvell H. F. and Fredericks P. M. (1997) Surface-enhanced Raman scattering of inorganic oxoanions. *Vib. Spectrosc.* **15**, 171–177.

Rosso K. M., Becker U. and Hochella, Jr., M. F. (1999) Atomically resolved electronic structure of pyrite 100 surfaces: an experimental and theoretical investigation with implications for reactivity. *Am. Miner.* **84**, 1535–1548.

Scaini M. J., Bancroft G. M., Lorimer J. W. and Maddox L. M. (1995) The interaction of aqueous silver species with sulphur-containing minerals as studied by XPS, AES, SEM, and electrochemistry. *Geochim. Cosmochim. Acta* **59**, 2733–2747.

Scott T. B., Allen G. C., Heard P. J. and Randell M. G. (2005) Reduction of U(VI) to U(IV) on the surface of magnetite. *Geochim. Cosmochim. Acta* **69**, 5639–5646.

Scott T. B., Riba Tort O. and Allen G. C. (2007) Aqueous uptake of uranium onto pyrite surfaces: reactivity of fresh versus weathered material. *Geochim. Cosmochim. Acta* **71**, 5044–5053.

Shannon R. D. (1976) Revised effective ionic radii and systematic studies of interatomic distances in halides and chalcogenides. *Acta Crystallogr.* **A32**, 751–767.

Sun Z., Forsling W., Rönngren L. and Sjöberg S. (1991) Surface reactions in aqueous metal sulfide systems: 1. Fundamental surface reactions of hydrous PbS and ZnS. *Int. J. Miner. Process.* **33**, 83–93.

Toniazzo V., Mustin C., Portal J. M., Humbert B., Benoit R. and Erre R. (1999) Elemental sulphur at the pyrite surfaces: speciation and quantification. *Appl. Surf. Sci.* **143**, 229–237.

Vaughan D. J., Becker U. and Wright K. (1997) Sulphide mineral surfaces: theory and experiment. *Int. J. Miner. Process.* **51**, 1–14.

Vergouw J. M., Difeo A., Xu Z. and Finch J. A. (1998) An agglomeration study of sulphide minerals using zeta-potential and settling rate: Part I. Pyrite and galena. *Miner. Eng.* **11**, 159–169.

Viollier E., Inglett P. W., Hunter K., Roychoudhury A. N. and Van Cappellen P. (2000) The ferrozine method revisited: Fe(II)/Fe(III) determination in natural waters. *Appl. Geochem.* **15**, 785–790.

Waite T. D., Davis J. A., Payne T. E., Waychunas G. A. and Xu N. (1994) Uranium(VI) adsorption to ferrihydrite: application of a surface complexation model. *Geochim. Cosmochim. Acta* **58**, 5465–5478.

Weerasooriya R. and Tobschall H. J. (2005) Pyrite–water interaction: effects of pH and pFe on surface charge. *Colloids Surf. A* **264**, 68–74.

Wersin P., Hochella, Jr., M. F., Persson P., Reden G., Leckie J. O. and Harris D. W. (1994) Interaction between aqueous uranium (VI) and sulfide minerals: spectroscopic evidence for sorption and reduction. *Geochim. Cosmochim. Acta* **58**, 2829–2843.

Associate editor: David J. Vaughan